RSC Applied Polymers

PAPER

View Article Online
View Journal | View Issue

Cite this: *RSC Appl. Polym.*, 2026, **4**, 1086

Low band gap π-conjugated porous polymers as bifunctional photoelectrocatalysts for overall water splitting

Bantumelli Prachuritha, Pranav Utpalla, Dasari Sai Hemanth Kumar and Krishnamurthi Muralidharan *

Conjugated microporous polymers (CMPs) are gaining attention for their unique structural properties and impressive charge transfer in electrochemical reactions. They are efficient bifunctional photoelectrocatalysts for crucial processes like the oxygen evolution reaction (OER), hydrogen evolution reaction (HER), and overall water splitting reaction (OWSR). The challenge in designing CMPs is achieving precise control of p-type and n-type behaviours within the polymer chain for specific photoelectrocatalytic reactions. We synthesized CMPs *via* Schiff-base condensation, tailoring their semiconducting properties and achieving band gaps under 1.6 eV by adjusting the acceptor to donor (A/D) ratio during synthesis. The CMP (designated as PDM1:2) with high donor content showed excellent properties for photoelectrocatalysis. It featured a semicrystalline morphology, resulting in impressive Tafel slopes (33 mV dec^{-1} for the OER, 122 mV for the HER) and overpotentials (η_{10}) (230 mV for the OER, 229 mV for the HER, and 1.69 V for the OWSR). The CMPs showed better catalytic performance under light and consistently performed over 500 cycles with excellent stability for 24 hours. These findings emphasize the importance of optimizing the A/D molar ratio in the polymer framework to improve the separation and migration of photogenerated charge carriers. This optimization led to improved photoelectrocatalytic performance for prolonged OWSRs. We developed a prototype exhibiting the bulk photoelectrocatalytic behaviour of our CMPs in facilitating the OWSR.

Received 14th December 2025,
Accepted 11th March 2026

DOI: 10.1039/d5lp00398a

rsc.li/rscapplpolym

1. Introduction

Electrochemical energy conversion and storage technologies, including water electrolyzers, fuel cells, and batteries, are expected to continue evolving in the near future.[1] Therefore, the demand for affordable and efficient energy systems that utilize sustainable and renewable sources is increasingly urgent. In this context, hydrogen stands out as a promising energy carrier that has the potential to tackle the growing energy crisis and the accompanying environmental challenges.[2,3] Traditionally, hydrogen production has relied on conventional methods, including natural gas reforming, coal gasification, and steam methane reforming. However, these processes primarily depend on non-renewable energy sources and emit greenhouse gases, drastically contributing to carbon footprints.[4] In contrast, electrochemical water splitting presents a promising, environmentally friendly, and sustainable method for hydrogen generation under ambient conditions.[5]

Requisite conditions for the synchronized evolution of hydrogen (H_2) and oxygen (O_2) in water electrolysis pose significant challenges primarily due to the considerable energy barriers, elevated overpotentials, and sluggish kinetics associated with the oxygen evolution reaction (OER) relative to the hydrogen evolution reaction (HER). Consequently, the OER plays a crucial role in energy conversion and storage systems, as it fundamentally determines the cost and overall efficiency of these processes.[6–9] Researchers predominantly use noble metal oxides like RuO_2, IrO_2, and Pt/C as electrocatalysts for the OER and HER.[10] However, the scarcity and high costs of these noble metals severely limit their widespread use in practical applications. A promising approach for enhancing the efficiency of electrocatalysts involves integrating solar energy with electrochemical water splitting in a tandem configuration, positioning it as a viable alternative to conventional water electrolysis.[11,12] Significant advancements have been made in the study of inorganic semiconductors (ISs), including metal oxides and metal chalcogenides, as potential photoelectrocatalysts for the OER and HER.[11,12] Nonetheless, substantial limitations, such as inadequate light absorption in the visible range and elevated band gap energies, impede their practical application in photoelectrocatalysis.

School of Chemistry, University of Hyderabad, Hyderabad, 500046, India.
E-mail: murali@uohyd.ac.in

The light-harvesting capabilities and facile charge transport ability of porous organic polymers (POPs) pave the way to design potential photoelectrocatalysts optimally[13] for overall water splitting reactions (OWSRs). Their free electrons provide semiconducting properties that enable extensive optical absorption. Conjugated microporous polymers (CMPs), a specific subclass of POPs, have garnered considerable interest for their application in OWSRs due to their favourable attributes, such as a porous framework, an elevated surface area, a π-conjugated backbone, tuneable band gaps, and robust visible light absorption characteristics.[14] Furthermore, the presence of heteroatoms like N, P, S, B, and Si in CMPs enhances catalytic activity by modifying Fermi energy levels and local electronegativity.[15–17]

Many CMPs are prepared *via* coupling reactions using metal catalysts. However, metal-catalysed synthesis[18] of these polymers poses challenges, including elevated costs and potential complications with pore blockage and structural collapse after extended purification.[19] Mallik *et al.* theoretically studied the effects of heteroatom doping on graphene sheets for the oxygen evolution reaction.[20] Oaki *et al.* used machine learning to create metal-free electrocatalysts, benzoquinone (BQ) and benzoxazole (BO), for hydrogen evolution.[21] Liao *et al.* synthesized pyridyl-conjugated microporous polymers *via* a metal-free method for photocatalytic hydrogen evolution.[22] Li *et al.* introduced π-conjugated graphdiyne as an efficient hole-transporting material in photoelectrocatalysts.[23] Jayanthi *et al.* reported that incorporating nitrogen enhances the photoelectrochemical activity of semiconducting polymers.[24] Generally, lower band gaps with extended π-conjugated CMPs are effective in energy applications. However, examples of CMPs that can absorb a broader visible light spectrum with band gaps below 1.5 eV remain rare.[25]

Substantial efforts have been made to reduce the band gap by incorporating electron donor or electron acceptor moieties into the polymer structure and enhancing aromatic content by selecting aromatic monomers.[26–28] Additionally, the band gap energy can be tuned by varying the content of donor and acceptor monomers in the polymer chain, which also facilitates efficient charge separation and transfer. Schwarz *et al.* synthesized a series of sulphur and nitrogen-containing conjugated polymers, systematically adjusting the band gap, and investigated their effect on photocatalytic activity.[26] In a separate study, Zhao *et al.* created a set of polymers featuring pyrene as the electron donor unit (D) and dibenzothiophene sulfone as the electron acceptor unit (**A**). They showed the influence of the A/D ratio on photocatalytic performance by manipulating the electron acceptor content within the polymer compositions.[29] Among the strategies employed, the design and synthesis of nitrogen-rich polymers with adjustable A/D ratios are the most promising approach for achieving the desired band gap energy and enhancing photoelectrocatalytic activity. Therefore, there is an urgent necessity for a simple, cost-effective, and metal-free synthetic method to produce CMPs that captivate and deliver improved catalytic activity.

We aimed to produce various CMPs with precisely designed A/D ratios to achieve higher catalytic efficiency in the overall water splitting reaction (OWSR). Conventional synthesis of CMP materials involves the use of metal catalysts; thus, residual metal can affect the catalytic activity of CMPs. However, in this work, we have utilized a simple Schiff-base condensation reaction to synthesize nitrogen-rich π-conjugated CMPs, which are not contaminated by metal. Furthermore, we used a low-cost precursor, such as melamine, in the synthesis. This nitrogen-rich compound simultaneously introduces polar sites in the CMPs, which can improve electrolyte wettability and facilitate charge transfer through the polymer framework. The synthetic process utilizes the less expensive, commercially available nitrogen-rich monomer, 1,3,5-triazine-2,4,6-triamine (melamine) (M). By varying the stoichiometric ratio of melamine, acting as the electron donor unit (D), and pyrrole-2,5-dicarbaldehyde (PD), serving as the electron acceptor (A), we produced different sets of polymers [A : D molar ratios = 1 : 2 (PDM1:2), 1:1 (PDM1:1), and 2 : 1 (PDM2:1)] through a reaction involving no metal catalysts.

The synthesized polymers showed a promising ability to absorb visible light, with ideal band gap energies of less than 1.6 eV and effective charge separation. Notably, semiconducting melamine–pyrrole-based polymers with a band gap below 1.6 eV have not been previously synthesized or analysed for their photoelectrocatalytic applications. This motivated us to explore their photoelectrocatalytic activity, leading us to investigate the electrocatalytic capabilities of these conjugated microporous polymers (CMPs) in the OER, HER, and OWSR under both dark and visible light conditions. Our results revealed lower overpotentials and a higher electrochemical surface area, which highlighted the performance of these CMPs. We also examined the effect of the amine-to-dialdehyde (A/D) molar ratio in the CMPs on their photoelectrocatalytic performance. Our findings suggest that engineering the A/D ratio is crucial for optimizing their bifunctional catalytic applications. These insights provide a new direction for designing CMPs with tailored band gaps by adjusting the A/D ratios.

2. Experimental

2.1 Materials

Melamine (Sigma-Aldrich), dimethyl sulphoxide (AR dry solvent, Finar), ethanol (Accusol-95™), tetrahydrofuran (Finar), potassium hydroxide pellets (Finar, extra pure), Milli-Q water, nickel foam (The Electrode Store), and Nafion-117 solution (Nanochemazone) were purchased and used without further purification. Pyrrole 2,5 dicarboxaldehye was synthesized as per the reported procedure.[30]

2.2 Polymer synthesis

Pyrrole 2,5-dicarboxaldehyde (the acceptor), melamine (the donor), and 15 mL of dimethyl sulfoxide (DMSO) were added to a 50 mL two-neck round-bottom flask equipped with a water-cooled condenser and a magnetic stir bar. The reaction

flask was degassed using nitrogen, and the reaction mixture was heated at 180 °C for 72 hours. Once cooled to room temperature, the solid product was filtered using a Buchner funnel and washed with excess ethanol. It was further purified using Soxhlet extraction in tetrahydrofuran (THF) for 48 hours. The resulting powder was dried at 80 °C for 24 hours before being collected. Various stoichiometric ratios of the monomers—acceptor to donor (2:1, 1:2, and 1:1)—were employed to synthesize the corresponding imine-linked polymers, designated as PDM2:1, PDM1:2, and PDM1:1. The synthesized imine-linked polymers corresponding to the different A/D ratios of 1:2, 2:1, and 1:1 are referred to as PDM1:2, PDM2:1, and PDM1:1, respectively.

2.3 Instrumentation and sampling techniques

Fourier transform infrared (FT-IR) spectra were recorded using a Thermo Fisher Scientific model – Nicolet iS5 spectrometer. The solid-state ^{13}C cross-polarization magic angle spinning nuclear magnetic resonance spectrum (CP/MAS NMR) was recorded using a JEOL 400 MHz spectrometer at a spin rate of 10 kHz using a 4 mm MAS probe. Powder X-ray diffraction (PXRD) was recorded using a Bruker D8 X-ray diffractometer (Cu K_α = 1.54 Å; operating voltage = 40 kV; operating current = 30 mA) in the 2θ range of 10°–80°. The UV-vis diffuse reflectance spectra were recorded using a JASCO-V770 UV-vis spectrometer. Thin film samples were prepared to measure the steady-state fluorescence by evaporating the ethanol solution of the compound on a quartz substrate. The steady-state fluorescence spectra were recorded using a JASCO spectrofluorometer FP-8500. The excited state lifetime studies were performed using MicroTime 200, Symphotime; a 405 nm pulse-laser diode was used for the excitation.

Thermogravimetric analysis (TGA) has been carried out by using a PerkinElmer (Pyris STA 6000 model) thermogravimetric analyser in the temperature range of 30 °C–900 °C at a heating rate of 5 °C min^{-1} under the flow of nitrogen gas (20 mL min^{-1}). Differential scanning thermograms were recorded using a Mettler Toledo (DSC822^e) differential scanning calorimeter by scanning the polymer samples over 30 °C–400 °C at a scanning rate of 10 °C min^{-1} under nitrogen flow (50 mL min^{-1}). The polymer surface area and pore size distributions were analysed by nitrogen adsorption and desorption isotherms at 77 K using a Micromeritics ASAP 2020 surface area and porosity analyzer. Before analysis, all the polymer samples were degassed at 120 °C for 20 h under high vacuum. The Brunauer–Emmett–Teller (BET) method was employed to determine the surface area of the polymers. The Barrett–Joyner–Halenda (BJH) desorption analysis revealed the pore size distribution for the same. Field-emission scanning electron microscopy (FE-SEM) imaging was carried out using a Carl Zeiss model – Merlin Compact FE-SEM. Transmission electron microscopy (TEM) images were captured using a JEOL model – JEM-F200/F2 multipurpose electron microscope. The as-prepared compounds were dispersed in ethanol and sonicated for 30 minutes, and then drop-cast on carbon-coated copper grids (200 mesh) for analysis.

2.4 Measurements of catalytic activities

The photoelectrochemical measurements were carried out using the CHI6112E instrument coupled with a PiCO solar simulator (1 SUN output ~100 mW cm^{-2} under manufacturer calibration conditions) with an AM1.5G filter equipped with an LED lamp covering 400–1100 nm wavelength range. The light source was positioned at a fixed working distance of 7 cm (with light intensity ~100 mW cm^{-2} under manufacturer calibration conditions) from the active material in the electrochemical setup for all the experiments carried out under illumination conditions. Electrochemical measurements for the oxygen and hydrogen evolution reactions were carried out using a conventional three-electrode setup with the polymer-casted nickel foam as the working electrode, Hg/HgO as the reference electrode, and a Pt wire as the counter electrode, and all were dipped in 1.0 M aqueous KOH electrolyte. For overall water splitting, electrochemical measurements were carried out using a two-electrode setup where the active material coated on the nickel foam was used as the working and counter electrodes. To prepare the working electrode, the active material (5 mg) was dispersed in 800 μL of ethanol along with 1 mg of carbon black; 20 μL of Nafion was added to the mixture and sonicated at room temperature for 1 h to obtain a homogeneous polymer ink. The resulting polymer ink (40 μL) was drop-cast on the nickel foam and allowed to dry at 60 °C overnight. The electrochemical studies were conducted at 25 °C under darkness and visible light illumination. Studies were repeated three times to ensure accurate results, and the data represented the average of multiple trials.

The catalytic activity for the OER was assessed by conducting linear sweep voltammetry (LSV) across a potential range of 0.67 V to 1.67 V *versus* the reversible hydrogen electrode (RHE), with a scan rate of 5 mV s^{-1}. The electrode potentials were referenced to the RHE using the equation E (*vs.* the RHE) = E (*vs.* Hg/HgO) + 0.098 + 0.0591 × pH. The catalytic activity for the HER was assessed by conducting linear sweep voltammetry (LSV) over a potential range of −0.65 V to 0.3 V *vs.* the RHE, with a 5 mV s^{-1} scan rate. The cell potential for overall water splitting was recorded within the range of 0.8 V to 2 V. Tafel plots, depicting overpotential *versus* log current density (j), were derived from the LSV data through linear fitting in the faradaic region. The electrochemical stability of the polymers was evaluated using chronoamperometry over a period of 24 hours. Faradaic efficiency was determined using the volume displacement method within a two-electrode system, comprising working and counter electrodes. A gas chromatograph (PerkinElmer; Clarus690) assembled with a thermal conductivity detector (TCD) and nitrogen as a carrier gas was utilized to detect the produced gases in the overall water splitting reaction. The evolved gases were collected and injected into the GC column.

2.5 Electrochemical studies

Cyclic voltammetry (CV) was carried out at different scan rates (10 mV s^{-1}–100 mV s^{-1} in steps of 10 mV s^{-1}), and the slope of

the plot of Δj (Δj = anodic current density − cathodic current density) *vs.* the scan rate provided the double layer capacitance (C_{dl}). The electrochemical surface area (ECSA) of all the polymers was calculated from double-layer capacitance. Band gap energy of the polymers was calculated from CV, considering ferrocene system as the reference, while using the saturated calomel electrode (SCE) as the reference electrode. The CV was recorded at 50 mV s^{-1} scan rate, in anhydrous acetonitrile with 0.1 M tetrabutylammonium perchlorate as a supporting electrolyte and 5 mM ferrocene as an internal reference.

Electrochemical impedance spectroscopy (EIS) measurements were also carried out to determine the electrical conductivity of the synthesized electrocatalysts. EIS measurements were carried out in the frequency range of 1 Hz–100 kHz with a small modulation voltage of 0.01 V. Samples for EIS were prepared by drop-casting the polymer ink on the PEDOT:PSS-coated FTO (fluorine tin oxide) glass and allowed to dry at 60 °C overnight. Electrical contacts were made through a copper wire attached to the FTO glass substrate by using a silver paste. The Mott–Schottky (M–S) measurements, using a similar setup as EIS, were recorded at a frequency of 1000 Hz, maintaining a neutral pH level using 1 M Na_2SO_4. The linear fit of the M–S plot (C^{-2} *vs.* the applied potential) gives the slope of the curve, which relates to the donor concentration.

3. Results and discussion

3.1 Synthesis, characterization, and properties of CMPs

Synthesis. The design of polymers that incorporate A/D units not only alters their optical properties but also influences molecular interactions, backbone planarity, packing, and microstructure when coated on surfaces or deposited as thin films. Therefore, there is a pressing need for the sustainable synthesis of suitable CMPs with controlled A/D ratios to function as photoelectrocatalysts in the bulk OWSR without necessitating complex methodologies. In this regard, we have synthesized porous conjugated polymer networks by varying the molar ratios of PD and M through a straightforward Schiff-base condensation reaction (Scheme 1). The A : D molar ratios were adjusted to 1 : 2 (PDM1:2), 1 : 1 (PDM1:1), and 2 : 1 (PDM2:1). Notably, all synthesized polymers were found to be insoluble in water and various organic solvents, including methanol, THF, ether, and hexane, indicating the presence of a rigid backbone and 3D-network chains within the polymer structure.

Characterization. FT-IR spectral analysis (Fig. 1a) confirms the presence of key functional groups in the synthesized polymers. Specifically, the peak at 3004 cm^{-1} suggested the presence of the –N–H stretching vibration, and the peaks at 1653 cm^{-1} could be attributed to –C=N stretching. The peak at 1536 cm^{-1} corresponds to –C–N–C bending, while the presence of a triazine ring was observed at 1434 cm^{-1}. The peak at 1173 cm^{-1} was due to the –C–N stretching vibration. These characteristic FT-IR peaks confirmed the formation of imine-linked polymers. The molecular structure of the polymer skel-

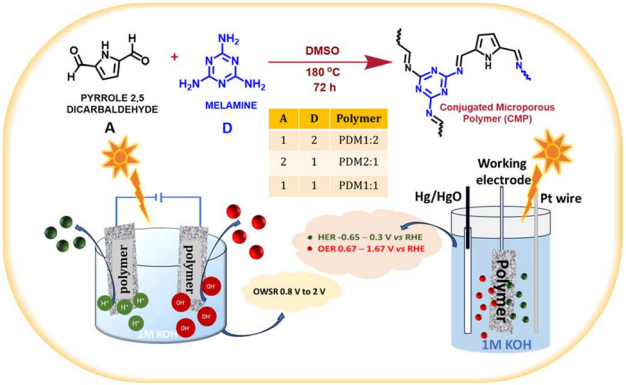

Scheme 1 Schematic representation for the synthesis of CMPs *via* Schiff-base condensation with varying A/D ratios (PDM1:2, PDM1:1, and PDM2:1) and their applications.

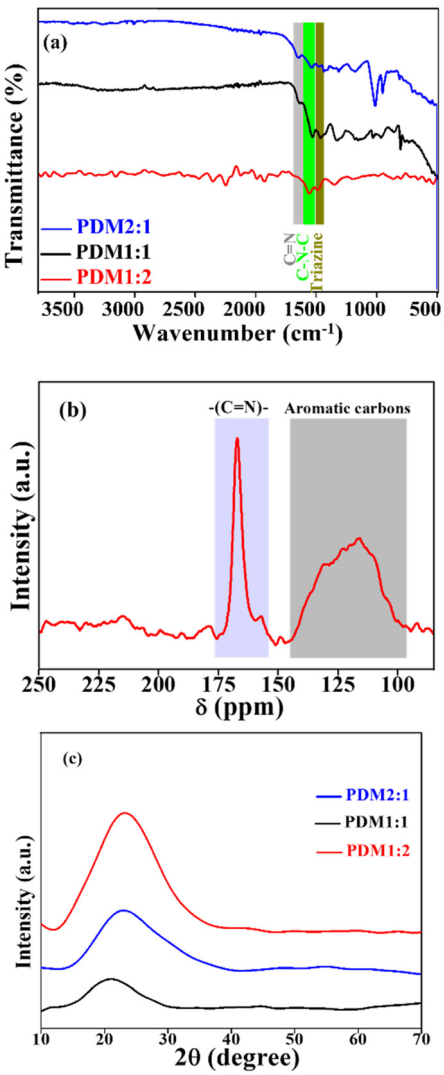

Fig. 1 (a) FT-IR spectra of PDM1:2, PDM1:1, and PDM2:1, (b) ^{13}C solid state NMR of PDM1:2, and (c) PXRD patterns for all the CMPs.

eton was determined using the ^{13}C CP/MAS solid-state NMR spectrum, with resonance peaks compared to those reported in the literature.[31,32] The resonance peak in the 100–135 ppm range was indicative of aromatic carbons within the polymer framework. A distinct resonance peak observed at 164 ppm could be attributed to the –C═N– imine group. Notably, the characteristic resonance peak for the aldehyde moiety at 190 ppm was absent, further confirming the complete polymerization of the monomers and the successful formation of the desired imine structures (Fig. 1b).

The crystalline and amorphous characteristics of the polymers were analysed using powder X-ray diffraction (PXRD) within a 2θ range of 10° to 70° (Fig. 1c). All the polymers exhibited diffuse peaks accompanied by a significant amorphous halo, indicating their semicrystalline nature. The broadness of the peaks was attributed to the small size of the crystallites. Among the samples, PDM1:1 displayed the highest amorphous fraction, as evidenced by the weakest peak intensity and the smallest peak area. In contrast, PDM1:2 exhibited a higher XRD peak intensity, suggesting a greater crystalline fraction, followed closely by PDM2:1. This observation aligns with the nominal composition of the acceptor (amorphous) and donor (crystalline) motifs present in the polymers. Additionally, slight shifts in the characteristic peak positions in the XRD results were attributed to changes in the electronic structure of the polymers as the A/D ratio varied.

Morphology and pore structure. The morphologies of all the polymers investigated through electron microscopy displayed aggregated crystallites with a disordered, porous structure (Fig. 2a–f). The average particle size was calculated from the TEM images using ImageJ software (Fig. S1 in the SI). Notably, the high-resolution TEM images and selected area electron diffraction (SAED) patterns for the polymers PDM2:1, PDM1:1, and PDM1:2 were distinctly different (insets of Fig. 2g–i). The high-resolution TEM images of PDM1:2 and PDM2:1 revealed clear fringes, while no fringes were detected for PDM1:1. This microscopic analysis further supports the presence of a more crystalline fraction in the polymer PDM1:2. An increase in the donor content (which includes a crystalline donor motif) within the polymer composition augmented its crystalline properties. The effects of enhanced crystallinity were reflected in the catalytic performance of the polymers, which will be discussed further.

The porous structure and surface area of the polymers were determined through nitrogen adsorption/desorption analysis at 77 K (Fig. 3(a–c)). Among the synthesized polymers, PDM1:2 exhibited a remarkable BET surface area of 428 $m^2\ g^{-1}$, whereas the surface areas for the other polymers, PDM2:1 and

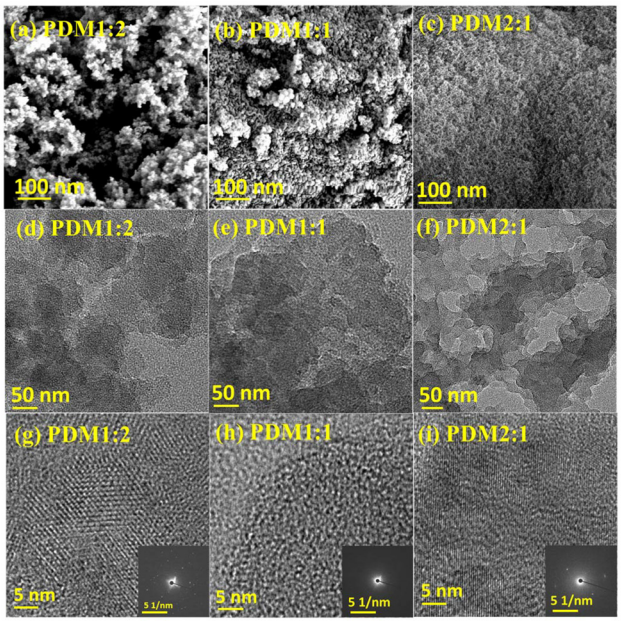

Fig. 2 (a–c) FESEM images, (d–f) TEM images, and (g–i) HRTEM images of PDM1:2, PDM1:1, and PDM2:1, respectively. The inset shows the corresponding SAED pattern of the polymers.

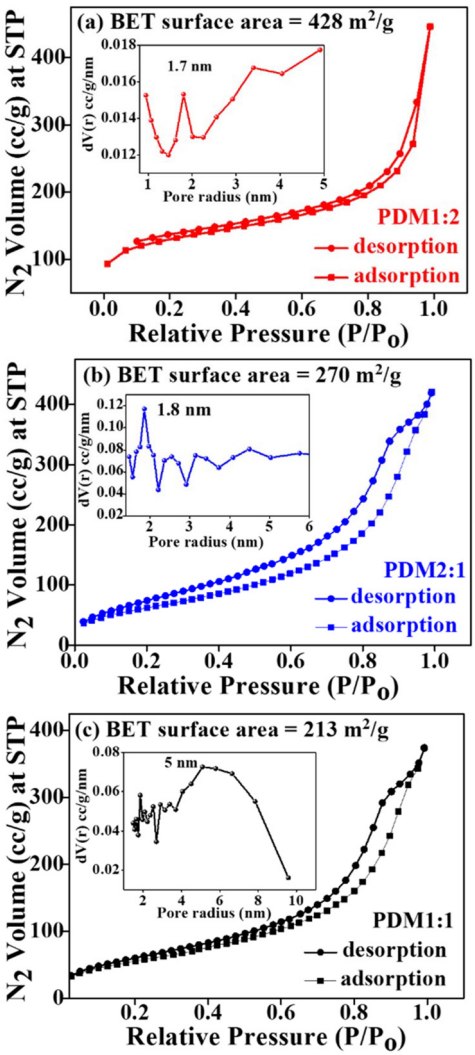

Fig. 3 (a–c) N_2 adsorption/desorption isotherms at 77 K for PDM1:2, PDM2:1, and PDM1:1. The inset shows the pore size distribution according to the BJH analysis.

PDM1:1, were 270 $m^2\ g^{-1}$ and 213 $m^2\ g^{-1}$, respectively. The higher surface area of the polymer PDM1:2 could be attributed to its higher content of the covalent triazine monomer, melamine. The pore size distribution, assessed using the Barrett–Joyner–Halenda (BJH) desorption analysis, indicates that both PDM1:2 and PDM2:1 possess a combination of micropores and mesopores, predominantly exhibiting microporous characteristics with average pore sizes of 1.7 nm and 1.8 nm, respectively. In contrast, PDM1:1 displays a mesoporous nature with an average pore size of 5 nm.

Thermal stabilities of CMPs. The DSC thermogram of the CMPs indicated their semicrystalline nature (Fig. 4a), evidenced by the presence of a distinct glass transition temperature (T_g) and a melting temperature (T_m). The T_m was determined at the peak of the melting endotherm. A larger crystallite size correlated with a higher T_m, while a smaller crystallite size corresponded to a lower T_m. The trend observed in the T_m values (Table 1) aligned with the variations in the crystallite size of the polymers, as confirmed by the average particle size distribution plot obtained from the TEM analysis (Fig. S1, SI). An excess of donor or acceptor motifs contributed to the formation of a polymer with a more rigid backbone and a greater crystalline fraction, resulting in a higher T_g (Table 1). The T_g for the PDM1:1 polymer was the lowest due to its more amorphous fraction and, consequently, a more flexible structure. In contrast, PDM1:2 exhibited the highest T_g, followed by the PDM2:1 polymer, which was consistent with the crystalline fraction typically found in semicrystalline polymers.

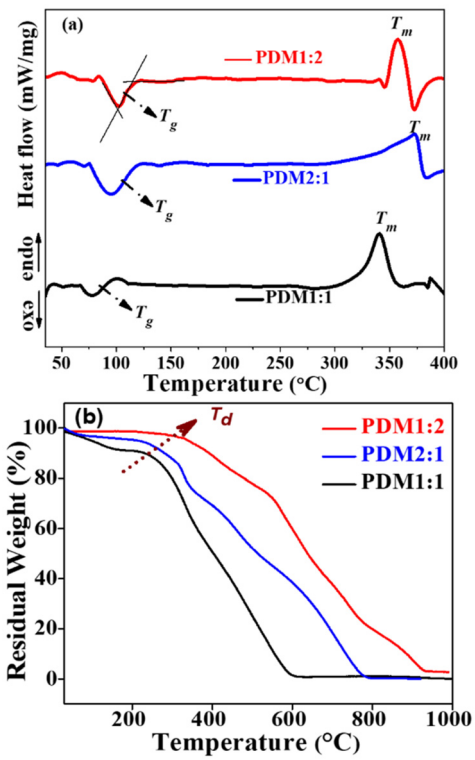

Fig. 4 (a) DSC thermograms and (b) TGA curves for the polymers PDM1:2, PDM2:1, and PDM1:1.

Table 1 T_g and T_m obtained from DSC thermograms; T_d calculated from TGA for the polymers PDM1:2, PDM1:1, and PDM2:1

Polymer	T_g (°C)	T_m (°C)	T_d (°C)
PDM1:2	109.6	356.3	323.6
PDM1:1	88.6	340.7	239.7
PDM2:1	107.2	370.3	246.8

Thermogravimetric analysis (TGA) conducted under a nitrogen atmosphere (Fig. 4b) indicated that the CMPs maintained thermal stability at elevated temperatures. The observed enhanced thermal stability can be attributed to the rigid polymer backbone, which induced a higher crystalline fraction. The initial weight loss observed in the TGA curves of the samples corresponds to the evaporation of the entrapped solvent within the polymer structure. As the temperature increased, the gradual weight loss reflected the progressive degradation of the semicrystalline polymers, primarily associated with their amorphous regions. The onset temperatures for polymer decomposition (T_d) for all samples are summarized in Table 1, indicating that PDM1:2 showed stability up to 323 °C. The higher T_d values for both PDM1:2 and PDM2:1, in comparison with PDM1:1, underscore the presence of a more rigid polymer backbone (indicating a higher crystalline fraction) in polymers with greater donor or acceptor compositions. Among the variants, PDM1:2 showcases the highest crystalline fraction, followed by PDM2:1, and then PDM1:1.

Absorption characteristics. To assess the photoelectrocatalytic activity of the polymers, we conducted UV-vis diffuse reflectance spectroscopy (UV-vis DRS), photoluminescence (PL), and time-resolved photoluminescence (TRPL) measurements. The absorption maxima (λ_{max}) for the CMPs PDM2:1, PDM1:2, and PDM1:1 were found to be 403 nm, 447 nm, and 487 nm, respectively. When the A/D ratio was 2:1 (more acceptor units), λ_{max} was 403 nm; however, when it was reversed (more donor units), the λ_{max} shifted bathochromically to 447 nm, highlighting the dependence on the acceptor/donor (A/D) ratio. Interestingly, when the A/D ratio was equal in PDM1:1, the highest λ_{max} for the polymer was noted at 487 nm. Fig. 5(a–c) display the UV-vis diffuse reflectance spectra of the polymers, with the inset illustrating the calculated optical direct band gap. The optical band gaps, determined *via* the Tauc plot, were found to be 1.56 eV for PDM2:1, 1.31 eV for PDM1:2, and 1.25 eV for PDM1:1. The variations in the band gap across different polymer compositions confirm the capability to tailor the band gap by changing the A/D motif ratio in the polymer backbone.

Consistent with the absorption spectra, the emission spectra (Fig. 5d) exhibited a notable shift in the emission maxima corresponding to the changes in the A/D ratio of the CMPs. The observed emission maxima were 419 nm, 461 nm, and 501 nm for PDM2:1, PDM1:2, and PDM1:1, respectively. Additionally, the PL emission intensities for PDM1:2 and PDM1:1 were significantly suppressed compared to PDM2:1, consistent with the particle size determined using TEM analysis. In nanomaterials with less particle size, there is a more

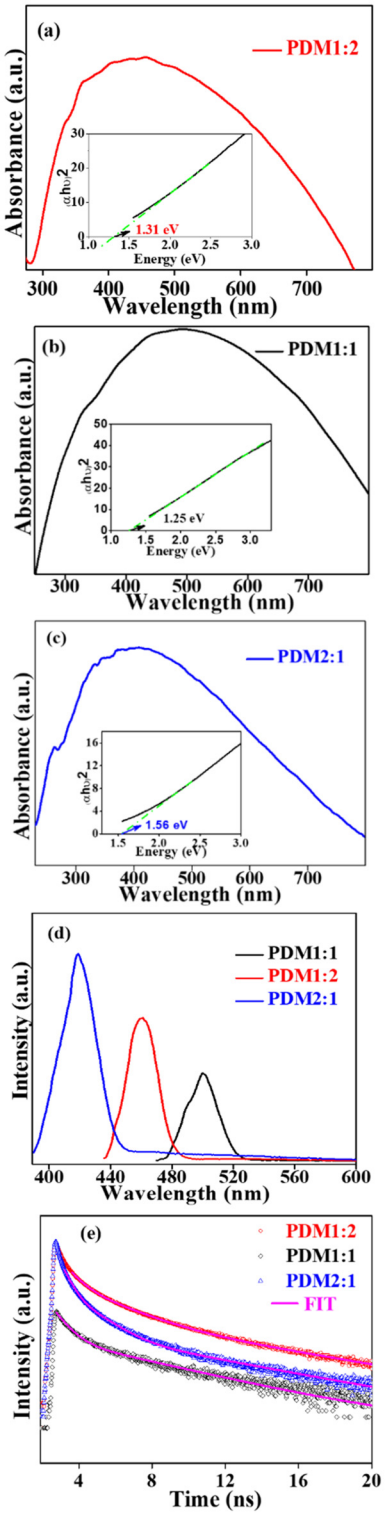

Fig. 5 (a–c) UV-vis DRS spectra of the polymers (inset: Tauc plot); (d) PL spectra of the polymers (λ_{ex} of PDM2:1, PDM1:2, and PDM1:1 was 395, 437, and 477 nm, respectively); and the (e) TRPL decay curves of the polymers. Line passing through the data points is the triexponential fit used for the calculation of lifetimes.

surface area-to-volume ratio and hence more possibility of surface effects, where non-radiative recombination of charge carriers occurs at the surface *via* surface states, resulting in reduced PL intensity. This phenomenon was further corroborated by the time-resolved photoluminescence (TRPL) decay curves.

Time-resolved photoluminescence is frequently employed to investigate carrier dynamics in semiconductors, offering valuable insights into carrier recombination mechanisms and lifetime. The TRPL decay curve for the polymers, illustrated in Fig. 5e, has been fitted with a triexponential decay function corresponding to three distinct lifetimes, as detailed in Table S1 (SI). The shorter lifetime (τ_s) is attributed to the Shockley–Read–Hall (SRH) non-radiative processes, indicating rapid recombination through defect trapping. The intermediate lifetime (τ_i) represents the charge separation process involving a mix of radiative and non-radiative processes. In contrast, the longer lifetime (τ_l) is likely linked to non-radiative Auger recombination or energy transfer through the radiative recombination of a free electron–hole pair.[33,34]

The shorter lifetime (τ_s) was the highest in PDM1:2 at 0.571 ns and in PDM2:1 at 0.511 ns, while it was the lowest in PDM1:1 at 0.419 ns. This suggests that recombination due to defect trapping was less pronounced in PDM1:2 compared to PDM1:1. This finding was consistent with the relative crystalline fraction observed in the composite materials, as determined through the XRD and thermal studies. The intermediate lifetime (τ_i) also exhibited varying trends: PDM1:2 at 2.656 ns, PDM1:1 at 1.559 ns, and PDM2:1 at 0.787 ns. Furthermore, the longer lifetime (τ_l) was the lowest in PDM1:2 at 3.092 ns and the highest in PDM1:1 at 5.060 ns, indicating that the rates of Auger recombination or charge transfer were higher in PDM1:2 in comparison with PDM1:1.

The weighing factors/amplitudes (pre-exponential factors: B_s, B_i, and B_l) showed the relative predominance of different recombination mechanisms in the CMPs. In the case of PDM1:2, the longer lifetime component was predominant, suggesting that Auger recombination or energy transfer played a significant role as a recombination mechanism, resulting in the TRPL intensity (Fig. 5e). Conversely, the polymers PDM2:1 and PDM1:1 exhibited shorter lifetimes associated with SRH/non-radiative recombination due to defect trapping. Consequently, the influence of longer lifetimes was diminished, leading to lower intensities in the TRPL spectra. The average fluorescence lifetimes (τ_{avg}) for the polymers were measured at 0.6 ns for PDM2:1, 1.3 ns for PDM1:2, and 1.1 ns for PDM1:1. The extended fluorescence lifetime of PDM1:2 indicated a reduced rate of electron–hole pair recombination and improved charge separation efficiency. Thus, the variation in lifetimes among the synthesized CMPs contributed to differences in the separation and transfer efficiency of photogenerated electron–hole pairs, providing valuable insights for predicting the performance of their photoelectrocatalytic activity.[29,31]

The band edge positions of the polymers, determined through cyclic voltammetry using a three-electrode system,

revealed that the polymers PDM2:1, PDM1:2, and PDM1:1 exhibited onset oxidation and reduction potentials of 0.47 V & −0.95 V, 0.24 V & −1.12 V, and 0.22 V & −1.05 V (*vs.* SCE), respectively (Fig. S2 in the SI). The highest occupied molecular orbital (HOMO) and lowest unoccupied molecular orbital (LUMO) energy levels were calculated relative to the reference ferrocene system, as detailed in Table S2 (SI). The calculated electrochemical band gaps (E_g) were found to be 1.42 eV, 1.36 eV, and 1.27 eV for PDM2:1, PDM1:2, and PDM1:1, respectively. The trend observed in the variation of E_g aligned closely with the optical band gaps obtained from the UV-vis Tauc plot. It is worth noting that the optical band gap is generally lower than the electronic band gap due to the additional coulombic interactions between the excited electrons and holes. Thus, the synthesized CMPs exhibited a promising ability to absorb visible light, characterized by a lower band gap and effective charge separation.

3.2 Oxygen evolution reaction (OER) studies

The current density (mA cm^{-2}) *vs.* potential (V) characteristics was determined using linear sweep voltammetry (LSV) with a three-electrode configuration. The polarization curves revealed overpotentials (η_{10}) for the polymers PDM2:1, PDM1:2, and PDM1:1 (under dark conditions) at 289 mV, 240 mV, and 270 mV, respectively. In contrast, the overpotential for bare nickel foam (NF) was 370 mV (Fig. 6a), significantly higher than that of the synthesized polymers, highlighting the enhanced electrocatalytic activity of the CMPs. Ni foam was employed as a current collector owing to its porous structure, better conductivity, and stability under alkaline conditions.[35] Other inert substrates, such as carbon materials, are prone to corrosion under alkaline conditions, hindering prolonged operation.[36]

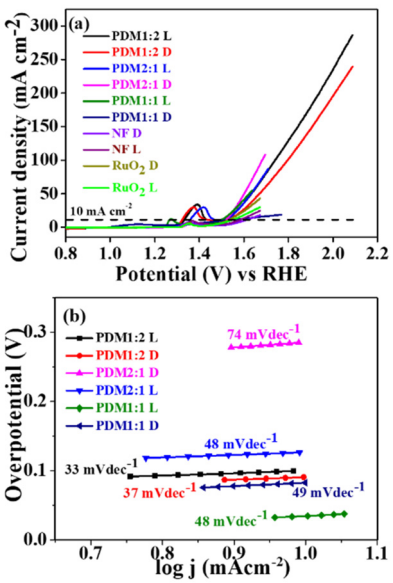

Fig. 6 (a) LSV curves for the OER (D and L represent dark and light conditions, respectively). (b) Tafel plots of polymers PDM1:2, PDM2:1, and PDM1:1 under dark and illumination conditions.

The electrocatalytic performance of the benchmark material RuO_2 was also assessed for direct comparison. At the same current density of 10 mA cm^{-2}, the overpotential for RuO_2 was measured at 310 mV, which was 70 mV higher than that of PDM1:2. This indicates the considerable potential of our CMPs for widespread applications in the photoelectrocatalytic OER. In the polarization plot for bare NF, the anodic peak at 1.34 V corresponds to the oxidation state transition from Ni^{2+} to Ni^{3+}, a feature that was consistently observed in all LSV plots for NF-supported electrocatalysts.[37] The direct impact of the high donor content within the CMP structure on reducing overpotential was particularly evident in the case of PDM1:2. The elevated donor content lowers the HOMO–LUMO energy levels, thereby reducing the band gap. Notably, there was a non-monotonous increase in the band gap relative to the OER activity of the polymers.

The overpotential (η_{10}) values obtained for the synthesized CMPs were lower than those reported in the literature, as summarized in Table S3 (SI). Notably, this includes metal-coordinated CMPs with an η_{10} of 400 mV,[38] triazine-based donor–acceptor conjugated polymers with an η_{10} of 328 mV,[39] N-doped mesoporous nanocarbon foams at 410 mV,[40] and Cu-CMP850 with an η_{10} of 350 mV.[41] Interestingly, a further reduction in η_{10} for all CMPs was observed under visible light illumination, with values measuring 260, 230, and 250 mV for the polymers PDM2:1, PDM1:2, and PDM1:1, respectively, as shown in Fig. 6a. While bare NF displayed an η_{10} of 340 mV and RuO_2 displayed 290 mV under visible light illumination, these results underscore the effectiveness of our CMPs in catalysing the reaction. This was further corroborated by the lower Tafel slope values of the polymers and the higher electrochemical surface area (ECSA) observed.

The electrocatalytic activity observed under illumination was revealed by a reduction in the Tafel slope for each polymer sample. Specifically, the Tafel slope values for the polymers PDM2:1, PDM1:2, and PDM1:1 changed from 74 to 48 mV dec^{-1}, 37 to 33 mV dec^{-1}, and 49 to 38 mV dec^{-1}, respectively, under illumination, as illustrated in Fig. 6b. The lower Tafel slope values signify an increase in catalytic activity. These findings indicated a highly promising application of the synthesized polymers for photoelectrocatalytic activity in the OER and address the longstanding challenge of elevated overpotential in OER catalyst materials.

The electrochemical surface area (Table 2) was determined using cyclic voltammetry (CV) at various scan rates (refer to Fig S3 in the SI) by estimating the double-layer capacitance (C_{dl}), as illustrated in Fig. 7a (a more detailed explanation of the ECSA estimation can be found in the SI). The higher ECSA indicates a greater presence of active sites available for catalytic activity. Notably, ECSA values were higher under illumination compared to dark conditions, showing an enhanced photoelectrocatalytic activity of the polymers when exposed to light.

The electrochemical stability of the polymers was investigated using the chronoamperometry technique. A constant potential of 0.6 V *vs.* the RHE was applied to the three-electrode system, and the resulting current was measured over

Table 2 The overpotential (η_{10}) and ECSA of the polymers PDM2:1, PDM1:2, and PDM1:1

	PDM2:1		PDM1:2		PDM1:1	
	Dark	Light	Dark	Light	Dark	Light
OER						
η_{10} (mV)	289	260	240	230	270	250
ECSA (cm^2)	9.3	12.2	11.1	19.3	10.7	19.1
HER						
η_{10} (mV)	279	250	252	229	281	274
ECSA (cm^2)	9.1	13.12	26.4	35.2	6.4	12.53

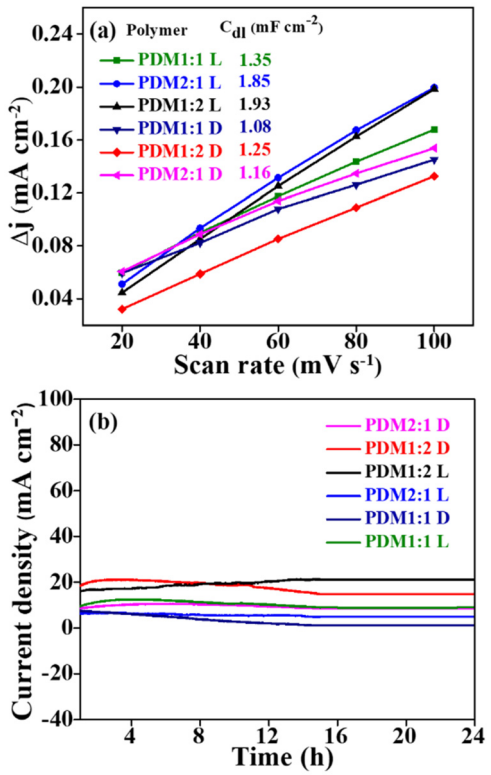

Fig. 7 (a) Plots for the estimation of double-layer capacitance (C_{dl}). (b) Chronoamperometric plots for the OER at 0.6 V under both dark and illumination conditions for all the polymers.

24 hours. All the CMPs showed a consistent current throughout the duration (Fig. 7b), confirming their electrochemical stability. The polymers exhibited reliable photoelectrocatalytic performance, with minimal variations in the overpotential (@10 mA cm^{-2}) observed before and after the chronoamperometry measurements over 24 hours (Fig. S4 in the SI). Furthermore, the synthesized CMPs exhibited similar overpotential values even after 500 cycles of cyclic voltammetry (CV), compared to the initial overpotential, reinforcing their excellent electrochemical stability (Fig. S5 in the SI). The polymers displayed a uniform morphology before and after the photoelectrochemical studies, as evidenced by the SEM images, further validating their stability and suitability for prolonged catalytic applications (Fig. S6 and S7 in the SI).

We assessed the catalytic activity of CMPs by measuring their faradaic efficiency (% FE) through volumetric analysis of the oxygen gas produced under dark and illumination conditions under a constant current of 20 mA (Fig. 8a & b). The results revealed a notable increase in faradaic efficiency for all the CMPs exposed to light, highlighting their photocatalytic capabilities. PDM1:2 exhibited the highest faradaic efficiency under both dark and illumination conditions, aligning with the increased donor concentration in the polymer composition. This finding supports the extended lifetime (τ_1) contribution in PDM1:2, indicating superior charge transfer efficiency. A higher donor ratio resulted in greater faradaic efficiency, whereas an increase in acceptor composition within the polymer led to a decline in efficiency. The photographic illustration quantifying oxygen gas in the customized bulk electrolysis setup can be found in Fig. S8 (SI), highlighting the effectiveness of the catalysts for the photoelectrocatalytic OER.

3.3 Hydrogen evolution reaction (HER) studies

The evaluation of the electrocatalytic activity for the HER using CMPs revealed promising results. Typically, the HER is conducted in acidic environments because it transpires faster. However, acidic conditions have drawbacks, such as reduced catalyst durability and effectiveness over extended periods. On the other hand, conducting the HER in alkaline or neutral environments can avoid these issues.[42] This study examined how well the prepared conjugated microporous polymers (CMPs) work as catalysts for the HER in a 1 M KOH alkaline

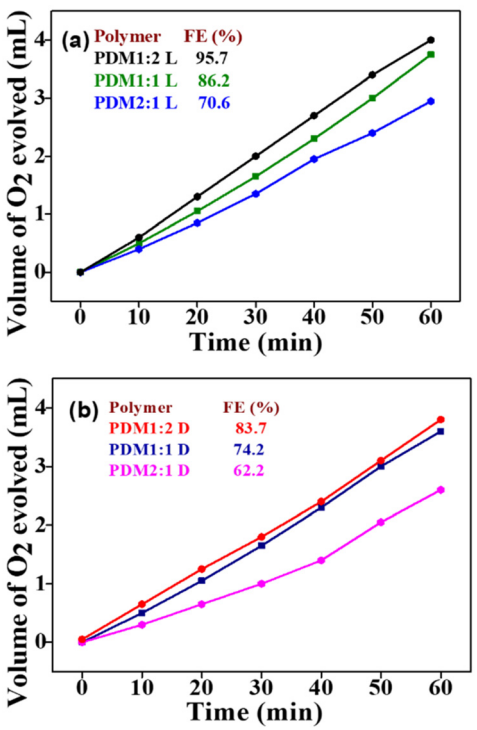

Fig. 8 Faradaic efficiency plots of polymers PDM1:2, PDM1:1, and PDM2:1 under (a) illumination and (b) dark conditions.

solution. This approach aims to find alternatives to platinum group metals (PGMs) for utility as efficient catalysts. The results showed that the synthesized CMPs significantly reduced the energy needed for the reaction when exposed to visible light.

The linear sweep voltammograms of PDM1:2, PDM2:1, and PDM1:1 recorded under dark conditions showed overpotential values (@10 mA cm^{-2}) of 252 mV, 289 mV, and 281 mV, respectively. In comparison, the overpotential for the bare nickel foam (NF) was 296 mV (Fig. 9a), which was significantly higher than that of the CMPs, highlighting their enhanced electrocatalytic activity. At the same current density, the overpotential of Pt/C was determined to be 133 mV. The overpotential values obtained were superior to those reported in the literature (see Table S4, SI). When light was applied, a further reduction in the overpotential values was observed. The polymers PDM1:2, PDM2:1, and PDM1:1 exhibited overpotentials of 229 mV, 250 mV, and 282 mV, respectively, at the same current density. This further confirmed the photo-responsive behaviour of the polymers.

Electrokinetic studies provided insights into the enhanced catalytic activity towards the HER. A key indicator of reaction kinetics is the Tafel slope: a lower slope suggests faster kinetics. Notably, the Tafel slope values observed under illumination decreased (from 163 to 122 mV dec^{-1} for PDM1:2, from 225 to 132 mV dec^{-1} for PDM2:1, and from 256 to 219 mV dec^{-1} for PDM1:1). This decrease confirmed that the reaction rate was significantly higher under illumination compared to that under dark conditions (see Fig. 9b). Furthermore, the Tafel slope values elucidated the trend in catalytic activity,

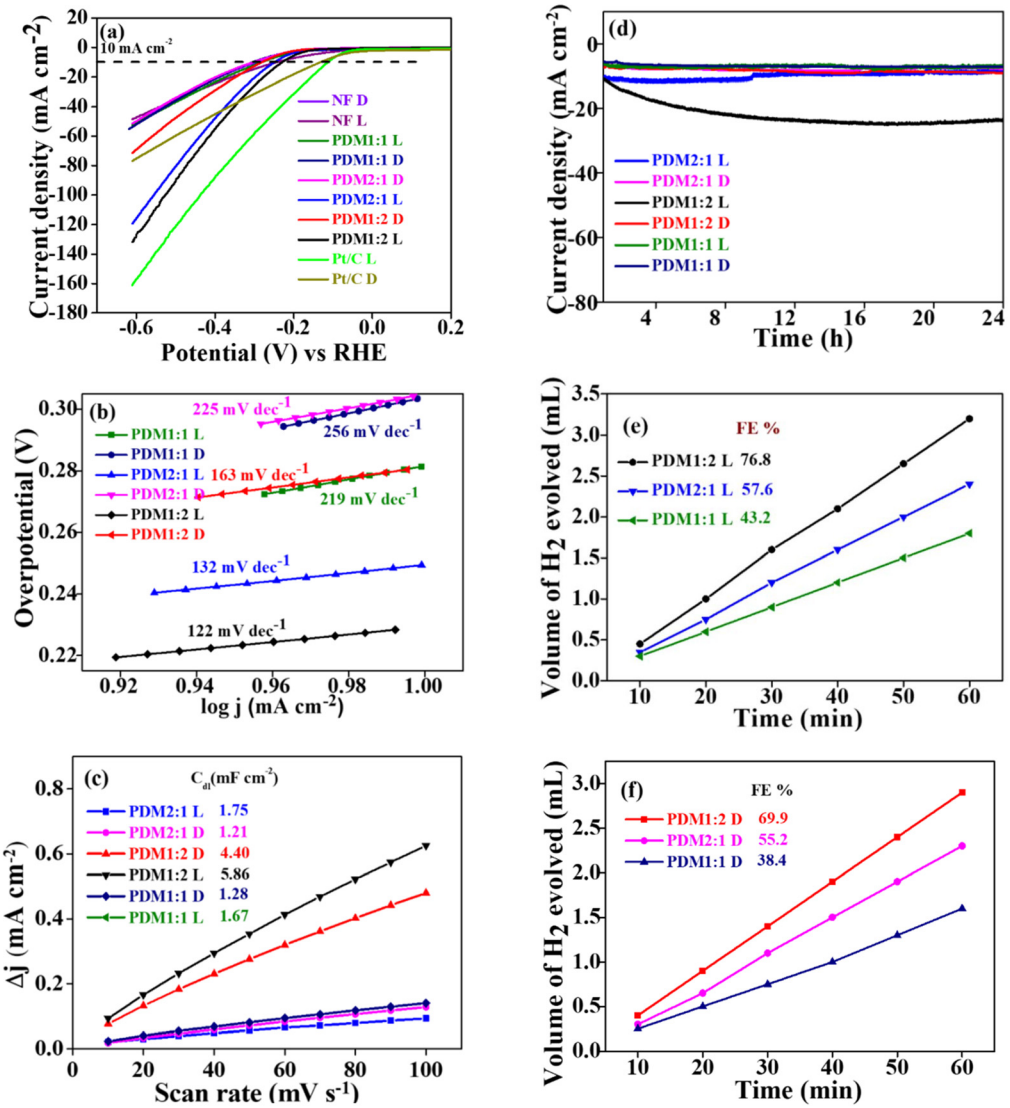

Fig. 9 (a) LSV curves for the HER. (b) Tafel plots of polymers PDM1:2, PDM2:1, and PDM1:1 under dark and illumination conditions, respectively. (c) Plots for the estimation of double-layer capacitance (C_{dl}). (d) Chronoamperometric plots for the HER at 1.1 V. (e and f) Faradaic efficiency plots of polymers PDM1:2, PDM1:1, and PDM2:1 under illumination and dark conditions, respectively.

which was the highest for PDM1:2, followed by PDM2:1 and PDM1:1.

Similar to the performance observed for the OER, the ECSA values measured at varying scan rates (10 to 100 mV s^{-1}) (Fig. S9) indicated an enhanced catalytic activity for the HER. Stability tests conducted at a constant potential of 1.1 V *vs.* the RHE showed that CMPs maintained their effectiveness in an alkaline environment over an extended duration of 24 hours. Furthermore, the analysis of overpotential at a current density of 10 mA cm^{-2}, both before and after chronoamperometry, confirmed the consistent photoelectrocatalytic performance of the CMPs (Fig. S10). Microscopic assessments indicated that there were no significant morphological changes after 24 hours of testing (Fig. S11). Additionally, the faradaic efficiency for the HER at 10 mA was found to be notably high for the CMPs, further underscoring their potential as effective catalysts.

3.4 Overall water splitting reaction (OWSR) studies

Utilizing the same electrocatalyst for both anode and cathode present several advantages over employing different electrocatalysts for the OWSR. When various active materials are involved in the OWSR, they are susceptible to unwanted parasitic reactions, cross-contamination, and dissolution of electrode materials. These issues can be mitigated using a uniform active material for both the anode and cathode. Additionally, a bifunctional catalyst minimizes the need for separate synthesis processes for two different catalysts, along with reducing equipment requirements and overall costs.[43] The remarkable electrocatalytic performances of our CMPs for the OER and HER, observed under both dark and illumination conditions, further inspired us to explore their overall OWSR activity in these environments.

The LSV measurements conducted under illumination conditions (Fig. 10a) showed lower cell potentials of 1.69, 1.78, and 1.79 V for the compositions PDM1:2, PDM2:1, and PDM1:1, respectively. In contrast, the cell potentials under dark conditions were 1.81, 1.85, and 1.83 V for the same polymers (Table 3). For the pristine nickel foam (NF), the cell potentials were recorded at 1.89 V in the dark and 1.87 V under illumination. The RuO_2//Pt–C exhibited cell potentials of 1.8 V in the dark and 1.78 V under illumination. These observations highlight the influence of increased donor content in the CMPs on their catalytic activity.

The evolution of hydrogen and oxygen gases was confirmed using gas chromatography (Fig. S12 in the SI). However, the optimal 2 : 1 molar ratio or peak area for $H_2 : O_2$ was not observed because H_2 has much higher thermal conductivity and thus a very high "relative response factor" than O_2 in the thermal conductivity detector used here. Hence, the H_2 peak area is disproportionately larger than O_2 because the detector is more sensitive to H_2. Other reason for the lower O_2 peak area might be the higher solubility of O_2 than H_2 in water, so that O_2 may remain dissolved in the electrolyte, or it may have been consumed in the surface oxidation of the electrode. Chronoamperometry studies (Fig. 10b) confirmed the electrochemical stability of the CMPs over 24 hours. Additionally, microscopic investigations revealed that the morphology of the polymers remained intact (Fig. S13 in the SI).

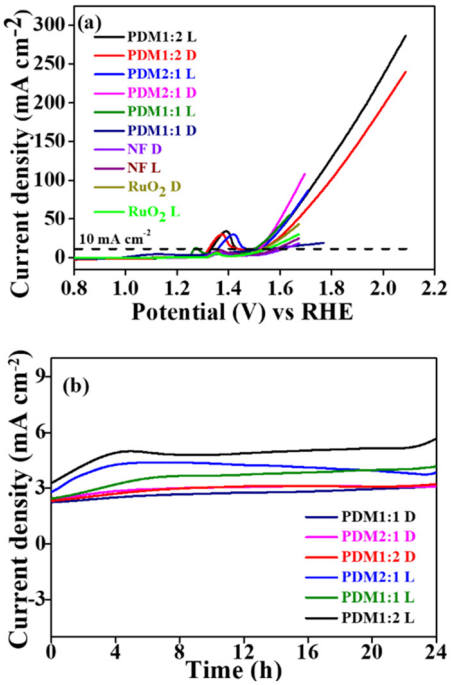

Fig. 10 (a) LSV plots towards the OWSR. (b) Chronoamperometric plots for the OWSR at 1.5 V for 24 h.

Table 3 Cell voltage in the OWSR (@10 mA cm^{-2}) for the polymers PDM2:1, PDM1:2, and PDM1:1

PDM2:1		PDM1:2		PDM1:1	
Dark	Light	Dark	Light	Dark	Light
1.85 V	1.78 V	1.81 V	1.69 V	1.83 V	1.79 V

Nyquist plots derived from the Electrochemical Impedance Spectroscopy (EIS) data (Fig. 11a) exhibited characteristics typical of semiconducting materials. The bulk resistance (Table S5 in the SI) was determined through semi-circular extrapolation of the Nyquist plot towards the real impedance axis, utilizing a suitable model circuit (inset in Fig. 11a). The PDM1:2 polymer displayed a significantly lower bulk resistance compared to PDM1:1 and PDM2:1 polymers, both under dark and illumination conditions. The conductivity (σ) of the CMPs was calculated (Fig. 11b) using eqn (1), where t is the thickness of the polymer coating, A is the coated area dipped in the electrolyte, and R is the bulk resistance of the polymer.

$$\sigma = \frac{t}{A \cdot R} \quad (1)$$

All CMPs showed higher conductivity under illumination compared to dark conditions, confirming their photo-responsive properties. Notably, the PDM1:2 composition exhibited

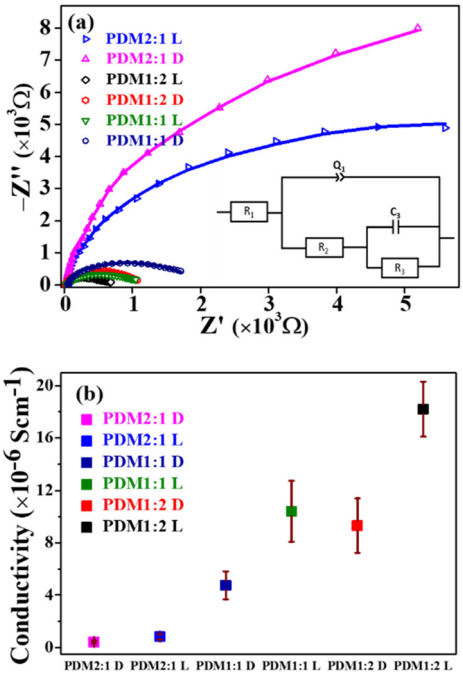

Fig. 11 (a) Nyquist plots and (b) conductivity of PDM1:2, PDMD1:1, and PDM2:1 under dark and illumination conditions (the inset in (a) shows the equivalent circuit diagram).

the highest conductivity at 1.82×10^{-5} S cm^{-1} under light. This increased conductivity corresponds to a higher catalytic activity, with PDM1:2 leading, followed by PDM1:1 and PDM2:1. The conductivity of the CMPs with a higher donor content remained significantly elevated even in the dark, surpassing the conductivity of PDM2:1 under illumination. This finding indicates that the relative acceptor/donor (A/D) ratio is a crucial determinant of inherent conductivity, taking precedence over external factors such as light conditions. This insight provides a pathway for optimizing the A/D ratio in conjugated polymers to achieve maximum conductivity for various electrochemical applications. The measured conductivity range (4.5×10^{-7} S cm^{-1} to 1.82×10^{-5} S cm^{-1}) falls within the typical values for semiconducting polymers, making them suitable for energy generation and storage devices.

To gain deeper insights into the semiconductor nature of the synthesized polymers, the Mott–Schottky (M–S) plot of the CMPs was recorded (Table S6 in the SI). This plot illustrates the relationship between space charge capacitance ($1/C^2$) and the applied bias potential.[44] The slope of the plot indicates the type of semiconductor present; an n-type semiconductor exhibits a positive slope, while a p-type semiconductor displays a negative slope. For the polymers PDM2:1, PDM1:1, and PDM1:2, both positive and negative slopes were observed simultaneously (S14 in the SI), indicating their p–n type semiconducting properties. This dual semiconducting nature (both p and n types) alters the Fermi levels, reduces the band gap energy, and enhances catalytic activity, thereby lowering the overpotential required for electrocatalytic processes. The slope of the M–S plot is inversely related to the dopant concentration (charge carrier density). A decrease in the positive slope was noted with an increase in donor concentration in the polymer PDM1:2, suggesting a higher donor doping density for this particular polymer, consistent with its nominal composition. This results in an increased charge carrier concentration in the conduction band.[45]

The intercept of the plot corresponds to the flat band potential, U_{fb}, which is the potential at which the band edges are flat, and there is no net charge accumulation. The flat band potentials (U_{fb}) for the polymers PDM1:2, PDM2:1, and PDM1:1 were −1.12, −0.92, and −1.03 V w.r.t. the NHE, respectively. The minimal difference observed between the flat band potentials and the conduction band edge values, derived from the cyclic voltammograms (see Fig. S2 in the SI), indicates a very low energy barrier for electron transfer across the interface, thereby highlighting the enhanced catalytic activity.

We have successfully shown a prototype that illustrates the bulk photoelectrocatalytic behaviour of our polymer in facilitating the overall water splitting reaction by connecting two AAA cells in series (Fig. S15 in the SI). This model has the potential to be scaled up for large-scale production of oxygen and hydrogen for energy generation and could be adapted into oxygen concentrators for use in remote areas. Consequently, our CMPs present a viable alternative to conventional inorganic materials for widespread applications.

3.5 Correlation between the A/D ratio, band gap, and electrochemical activity

We have chosen an equimolar acceptor (A)–donor (D) ratio as the control sample and investigated the two extremes: one with a double acceptor ratio and the other with a double donor ratio, to gain insights into the impact of the acceptor and donor in enhancing catalytic activity in our preliminary study. Our study established that the increased donor content within the polymer backbone significantly impacts photocatalytic activity. Initially, we expected that the PDM1:1 variant would exhibit more efficient catalysis compared to the other CMPs, PDM2:1 and PDM1:2, owing to its lower band gap of 1.25 eV and a greater bathochromic shift observed in UV–visible absorption. However, the polymer PDM1:2 exhibited a superior performance, despite having a band gap of 1.31 eV. The overpotential measured for PDM1:1 during the OER, HER and OWSR was higher than that of PDM1:2 under dark and visible light conditions. The enhanced catalytic performance of polymer PDM1:2 could be attributed to its optimal HOMO and LUMO energy levels, recorded at −0.24 V and 1.12 V (relative to the normal hydrogen electrode, NHE), respectively. This finding underscores the critical role of donor content in tuning the HOMO–LUMO energy levels necessary for efficient electrocatalytic activity.

The experimentally constructed energy band diagram illustrating the band gap energy and the calculated HOMO–LUMO energy levels relative to the vacuum and NHE for all CMPs is presented in Fig. 12. The findings showed that PDM1:2 exhibited a longer lifetime (as determined by the TRPL analysis), a

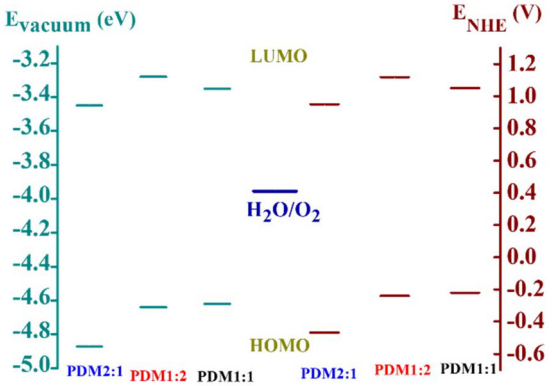

Fig. 12 The experimentally constructed energy band diagram representing the band gap energy and the HOMO–LUMO energy levels of the polymers PDM2:1, PDM1:2, and PDM1:1.

higher BET surface area, faster reaction kinetics (indicated by the Tafel slope), a greater ECSA, reduced charge transfer resistance, and enhanced electron flow (reflected in the flat band potential). These factors collectively suggest that increasing the donor content in the polymer structure significantly enhances the polymer's catalytic efficiency for the OER, HER and OWSR. These observations indicate that the effectiveness of a material's catalytic performance is not solely dictated by its broader visible light absorption or band gap energy, but rather depends on the relative HOMO–LUMO levels and the inherent charge transfer efficiency of the material.

4. Conclusions

We have synthesized a series of CMPs with varying stoichiometric ratios of acceptors and donors, and assessed their electrochemical and photoelectrochemical performances in the OER, HER, and OWSR. Among these, the variant PDM1:2, which contained a higher donor content in its backbone, exhibited exceptional performance. This behaviour can be attributed to the presence of polar sites, specifically donor atoms, which enhance the wettability of the electrolyte and facilitate charge transfer through the polymer framework. The incorporation of nitrogen heteroatoms can modify the electronic structure of the conjugated polymer backbone, thereby changing the band gap and revealing catalytically active sites. It achieved a lower band gap, enhanced absorption of visible light at longer wavelengths, an extended operational lifetime, and increased surface area. This research highlighted how variations in the acceptor–donor ratios influence the band gap and subsequently affect photoelectrochemical catalysis. Specifically, the best overpotentials (η_{10}) recorded for the OER were 240 mV and 230 mV, while for the HER they were 252 mV and 229 mV under dark and illumination conditions, respectively, while the cell voltages for the OWSR were 1.81 V and 1.69 V. The electrochemical tests under both dark and light conditions showed excellent stability over 500 activity cycles lasting 24 hours.

These findings position the examined CMPs among the most effective contemporary complementary metal–oxide–semiconductor materials, showcasing their potential for achieving lower overpotentials in the OER, HER, and OWSR. All findings suggest that changing the ratio of the constituents 'A' and 'D' in the CMPs affects important factors like the HOMO–LUMO energy levels, band gap, surface area, charge transfer resistance, and the efficiency of separation and migration of photogenerated charge carriers. These characteristics improve the performance of photoelectrocatalytic activity. This innovative approach could lead to large-scale production of hydrogen and oxygen, supporting clean energy systems. With some minor modifications, it could also serve as a life-saving oxygen concentrator in remote and underserved areas.

Author contributions

KM: conceptualization, funding acquisition, project administration, supervision, and writing – review & editing. BP: conceptualization, data curation, formal analysis, investigation, methodology, and writing – original draft. PU: visualization, validation, and writing – original draft. DSHK: resources and data curation.

Conflicts of interest

The authors declare no conflicts of interest.

Data availability

The data supporting this article have been included as part of the supplementary information (SI). Supplementary information: TRPL decay parameters, average particle size, electrochemical band gap calculations, HOMO–LUMO levels, overpotentials towards the OER, HER comparison table, ECSA calculation, EIS fit results, Mott–Schottky results, faradaic efficiency calculations, LSV stability, post-chronoamperometry analysis, and OWS prototype. See DOI: https://doi.org/10.1039/d5lp00398a.

Acknowledgements

The authors thank the Department of Science & Technology (DST), India, for project funding (DST/INT/RUS/RSF/P-38/2021 (G)) and fellowship. PU is thankful to the Institutions of Eminence (IoE) funds from the Ministry of Education, Government of India, towards the IoE-postdoctoral fellowship.

References

1 H. Zhao and Y. Lei, *Adv. Energy Mater.*, 2020, **10**, 2001460.
2 S. Chu and A. Majumdar, *Nature*, 2012, **488**, 294.

3 H. Jiang, Y. Sun and B. You, *Acc. Chem. Res.*, 2023, **56**, 1421–1432.
4 Y. Xu, M. Wu, X. Yang, S. Sun, Q. Li, Y. Zhang, C. Wu, R. E. Przekop, E. Romańczuk-Ruszuk, D. Pakuła and H. Zhou, *Carbon Capture Sci. Technol.*, 2023, **8**, 100129.
5 H. Sun, X. Xu, H. Kim, W. C. Jung, W. Zhou and Z. Shao, *Energy Environ. Mater.*, 2023, **6**, 12441.
6 G. Chen, Y. Sun, R. R. Chen, C. Biz, A. C. Fisher, M. P. Sherburne, J. W. Ager, J. Gracia and Z. J. Xu, *JPhys Energy*, 2021, **3**, 031004.
7 Z. F. Huang, J. Song, Y. Du, S. Xi, S. Dou, J. M. V. Nsanzimana, C. Wang, Z. J. Xu and X. Wang, *Nat. Energy*, 2019, **4**, 329.
8 B. You and Y. Sun, *Acc. Chem. Res.*, 2018, **51**, 1571–1580.
9 B. You, N. Jiang, M. Sheng, M. W. Bhushan and Y. Sun, *ACS Catal.*, 2016, **6**, 714–721.
10 S. Cherevko, S. Geiger, O. Kasian, N. Kulyk, J. P. Grote, A. Savan, B. R. Shrestha, S. Merzlikin, B. Breitbach, A. Ludwig and K. J. J. Mayrhofer, *Catal. Today*, 2016, **262**, 170–180.
11 F. E. Osterloh, *Chem. Soc. Rev.*, 2013, **42**, 2294.
12 X. Chen, S. Shen, L. Guo and S. S. Mao, *Chem. Rev.*, 2010, **110**, 6503.
13 L. Niu, L. Sun, L. An, D. Qu, X. Wang and Z. Sun, *MRS Bull.*, 2020, **45**, 562.
14 M. Barawi, L. Collado, M. Gomez-Mendoza, F. E. Oropeza, M. Liras and V. A. De la Peña O'Shea, *Adv. Energy Mater.*, 2021, **11**, 210150.
15 T. Mondal, M. G. Mohamed, M. F. Puthiyaparambath, R. Thapa and S.-W. Kuo, *ACS Appl. Energy Mater.*, 2026, **9**, 1790–1802.
16 K. M. Mithra, P. Govindaraj, S. S. V. Backiyaleela, H. Kim, S. Sinthika and R. Anand, *J. Mater. Chem. A*, 2026, **14**, 7121.
17 J. Gao, Y. Sun, N. Ma, Y. Chu, H. Wang, H. Tian, Z. Yin, X. Tan and P. Zhang, *Nanoscale*, 2026, **18**, 3698.
18 J. S. M. Lee and A. I. Cooper, *Chem. Rev.*, 2020, **120**, 2171.
19 J. Lee, O. Buyukcakir, T. W. Kwon and A. Coskun, *J. Am. Chem. Soc.*, 2018, **140**, 10937.
20 A. Priyadarsini and B. S. Mallik, *ACS Omega*, 2021, **6**, 5368.
21 W. Hamada, M. Hishida, R. Sugiura, H. Tobita, H. Imai, Y. Igarashi and Y. Oaki, *J. Mater. Chem. A*, 2024, **12**, 3294.
22 Q. R. Zeng, Z. H. Cheng, C. Yang, Y. He, N. Meng, C. F. J. Faul and Y. Z. Liao, *Chin. J. Polym. Sci.*, 2021, **39**, 1004.
23 J. Li, X. Gao, B. Liu, Q. Feng, X. B. Li, M. Y. Huang, Z. Liu, J. Zhang, C. H. Tung and L. Z. Wu, *J. Am. Chem. Soc.*, 2016, **138**, 3954.
24 S. Jayanthi, D. V. S. Muthu, N. Jayaraman, S. Sampath and A. K. Sood, *ChemistrySelect*, 2017, **2**, 4522.
25 H. Bohra, S. Y. Tan, J. Shao, C. Yang, A. Efrem, Y. Zhao and M. Wang, *Polym. Chem.*, 2016, **7**, 6413–6421.
26 D. Schwarz, Y. S. Kochergin, A. Acharjya, A. Ichangi, M. V. Opanasenko, J. Čejka, U. Lappan, P. Arki, J. He, J. Schmidt, P. Nachtigall, A. Thomas, J. Tarábek and M. J. Bojdys, *Chem. – Eur. J.*, 2017, **23**, 13023.
27 S. Bi, Z. A. Lan, S. Paasch, W. Zhang, Y. He, C. Zhang, F. Liu, D. Wu, X. Zhuang, E. Brunner, X. Wang and F. Zhang, *Adv. Funct. Mater.*, 2017, **27**, 1703146.
28 D. Lorcy and N. Bellec, *Chem. Rev.*, 2004, **104**, 5185.
29 H. Zhao, Y. Dong, P. Sun, Y. Bai, C. Ru, X. Wu, Z. Li, X. Han, J. Wu and X. Pan, *ACS Appl. Energy Mater.*, 2022, **5**, 4631.
30 G. M. Peters, J. B. Winegrad, M. R. Gau, G. H. Imler, B. Xu, S. Ren, B. B. Wayland and M. J. Zdilla, *Inorg. Chem.*, 2017, **56**, 3377.
31 N. Das, R. Paul, S. Biswas, R. Das, R. Chatterjee, A. Bhaumik, S. C. Peter, B. M. Wong and J. Mondal, *ACS Sustainable Chem. Eng.*, 2023, **11**, 2066.
32 W. B. Euler and J. E. Roberts, *Macromol*, 1989, **22**, 4221.
33 H. Zhang, J. Wei, J. Dong, G. Liu, L. Shi, P. An, G. Zhao, J. Kong, X. Wang, X. Meng, J. Zhang and J. Ye, *Angew. Chem.*, 2016, **128**, 14522.
34 D. Zanardo, G. Forghieri, E. Ghedini, F. Menegazzo, A. Giordana, G. Cerrato, E. Cattaruzza, A. Di Michele, G. Cruciani and M. Signoretto, *Molecules*, 2023, **28**, 4798.
35 X. Hu, X. Tian, Y. W. Lin and Z. Wang, *RSC Adv.*, 2019, **9**, 31563–31571.
36 L. A. Smith, K. Kawashima, R. A. Marquez and C. B. Mullins, *ACS Mater. Lett.*, 2024, **6**, 3190–3201.
37 A. Sivanantham, P. Ganesan and S. Shanmugam, *Adv. Funct. Mater.*, 2016, **26**, 4661.
38 Y. C. Kao, T. Mondal, W. H. Chang, M. G. Mohamed and S. W. Kuo, *Int. J. Hydrogen Energy*, 2025, **173**, 151390.
39 N. Gupta, S. Halder, R. P. Behere, P. Singh, S. Kanungo, M. Dixit, C. Chakraborty and B. K. Kuila, *ACS Appl. Mater. Interfaces*, 2023, **15**, 29042–29051.
40 J. Zhang, Z. Zhao, Z. Xia and L. Dai, *Nat. Nanotechnol.*, 2015, **10**, 444.
41 S. Cui, M. Qian, X. Liu, Z. Sun and P. Du, *ChemSusChem*, 2016, **9**, 2365.
42 T. B. Ferriday, P. H. Middleton and M. L. Kolhe, *Energies*, 2021, **14**, 8535.
43 L. Quan, H. Jiang, G. Mei, Y. Sun and B. You, *Chem. Rev.*, 2024, **124**, 3694.
44 T. Kutlusoy, S. Divanis, R. Pittkowski, R. Marina, A. M. Frandsen, K. Minhova-Macounova, R. Nebel, D. Zhao, S. F. L. Mertens, H. Hoster, P. Krtil and J. Rossmeisl, *Chem. Sci.*, 2022, **13**, 13879.
45 J. Bezboruah, D. M. Sanke, A. V. Munde, P. T. Bhattad, H. S. Karmakar and S. S. Zade, *Nanoscale Adv.*, 2023, **5**, 6670.